ChemComm

COMMUNICATION

View Article Online
View Journal | View Issue

Cite this: *Chem. Commun.*, 2025, **61**, 17641

Received 31st July 2025,
Accepted 26th September 2025

DOI: 10.1039/d5cc04382d

rsc.li/chemcomm

Ultrafast symmetry-breaking charge separation in thin films of J-aggregated perylenediimide multimers in a nonpolar solid-state environment

Aniruddha Mazumder, Kavya Vinod, Amalnadh T., Philip Daniel Maret, Ariharasudhan R. and Mahesh Hariharan *

We demonstrate ultrafast symmetry-breaking charge separation (τ_{CS} <110 fs) in thin films of J-aggregated perylenediimide (PDI) multimers in a nonpolar polymethyl methacrylate polymer matrix (ε = 2.80–3.20). Theoretical calculations reveal the role of through-space electronic communication and π–π interactions promoting ultrafast charge separation in PDI multimers in the solid-state.

Achieving efficient charge separation (CS) with minimal energy loss is a key challenge in advancing organic photovoltaic (OPV) devices.[1,2] Symmetry-breaking charge separation (SB-CS) has recently emerged as a prospective solution for generating hole–electron pairs in chromophoric assemblies without conventional donor–acceptor interfaces.[3,4] SB-CS takes advantage of asymmetry introduced by molecular packing or the surrounding environment to generate long-lived charge separated states (CSS) from photoexcited neutral chromophores, ultimately paving the way for improved open-circuit voltages and better device performance.[5–8] Although SB-CS is well documented in solution-phase systems where solvent polarity helps stabilize the charge separated state, achieving it in the solid-state, without the aid of external dielectric stabilization, presents both a fundamental challenge and a valuable opportunity for technological advancement.[1,9] Among the various π-conjugated systems explored, perylenediimides (PDIs) are outstanding electron-deficient chromophores known for their strong absorption, photostability, and high electron mobility.[10,11] Their excited-state dynamics are highly sensitive to molecular packing, and recent studies have shown that PDIs organized into solid-state multichromophoric assemblies can undergo SB-CS through intermolecular pathways.[12–15] Notably, SB-CS has been observed in the solid-state in systems where PDIs adopt slip-stacked geometries that promote through-space electronic coupling while suppressing excimer formation, otherwise leading to non-radiative losses.[13]

School of Chemistry, Indian Institute of Science Education and Research, Thiruvananthapuram, Maruthamala P.O., Vithura, Thiruvananthapuram, Kerala 695551, India. E-mail: mahesh@iisertvm.ac.in

Rational molecular design plays a crucial role in achieving such favourable packing geometries. Introducing bulky or directional substituents, tailoring the rigidity and conjugation of linkers, or using multimeric scaffolds can promote ordered slip-stacked aggregates in the solid-state.[12,15] These arrangements facilitate the electronic coupling necessary for SB-CS while simultaneously mitigating structural motifs that favour excimer formation.[13] Previously, we have shown that ultrafast intramolecular SB-CS can be achieved under the effect of polar solvents in angular PDI bichromophoric and trichromophoric structures through the modulation of intrachromophore electronic coupling.[16,17] Herein, we investigate the excited-state dynamics of two PDI-based multichromophoric assemblies (**PDI_2** and **PDI_3**) forming J-aggregated thin film structures. We demonstrate that such architectures enable ultrafast SB-CS even in a nonpolar polymethyl methacrylate (PMMA) polymer matrix, thus providing a framework for designing next-generation organic materials capable of efficient solid-state charge generation.

PDI_2 and **PDI_3** (Fig. 1a and b) were synthesized and characterized (Scheme S1 and Fig. S1–S8) following the previously reported procedures.[16,17] Key insights into the aggregate stacking were obtained using multi-dimensional NMR analyses in $CDCl_3$, where ~12 molecules of **PDI_2** and **PDI_3** each were estimated to be stacked in the individual aggregate structure (Fig. S9–S18; refer to SI for more details). The **PDI_2** optimized structure obtained at the B3LYP-D3/6-311+G(d,p) level of theory in vacuum, employing density functional theory (DFT), exhibited a core-twist of φ = 20.3° in the PDI fragment with bay-substitution (Fig. 1c). Meanwhile, the **PDI_3** optimized structure displayed core-twisting of both the terminal PDI fragments with φ = 20.6° (Fig. 1d).

The steady-state photophysical properties of **PDI_2** and **PDI_3** were investigated in thin films in a nonpolar PMMA matrix (ε = 2.80–3.20) in comparison to the photophysical properties at the monomer state in 1,4-dioxane (DIOX) at room temperature. The UV-vis absorption and fluorescence excitation spectra of

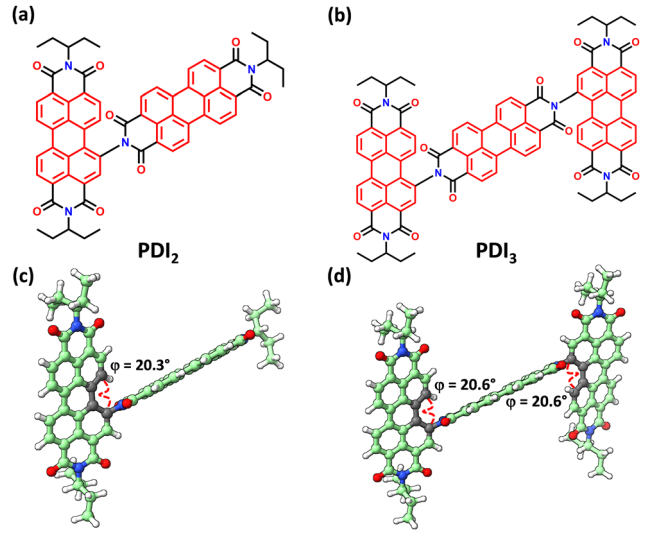

Fig. 1 Molecular structures of (a) **PDI$_2$** and (b) **PDI$_3$**. Optimized structures of (c) **PDI$_2$** and (d) **PDI$_3$** showing the core-twist in the PDI multimers.

PDI$_2$ and **PDI$_3$** thin films in PMMA reveal significantly broad red-shifted features compared to the **PDI$_2$** and **PDI$_3$** monomeric optical properties in DIOX (Fig. S19 and S20a). **PDI$_2$** thin film showed red-shifted broadened maxima in the excitation spectra (Fig. S19a) with $\lambda_{max}^{Exc} \approx 528$ nm (521 nm in DIOX), while **PDI$_3$** thin film exhibited broad maxima (Fig. S19b) at $\lambda_{max}^{Exc} \approx 521$ nm (516 nm in DIOX). The red-shifted excitation spectra of **PDI$_2$** and **PDI$_3$** thin films compared to the monomer excitation spectra in DIOX indicate the formation of J-type self-assembly in the aggregated state of **PDI$_2$** and **PDI$_3$**.[18,19] Moreover, the fluorescence emission spectra recorded for the **PDI$_2$** and **PDI$_3$** thin films in PMMA at room temperature exhibited red-shifted featureless emission profiles compared to the well-defined monomeric emission observed in DIOX (Fig. S19c, d and S20b).

Further, we have estimated the fluorescence quantum yields (ϕ_{FL}) of **PDI$_2$** and **PDI$_3$** to probe the emissive nature of the PDI dimers in a closely packed solid-state arrangement. **PDI$_2$** and **PDI$_3$** showed reduced ϕ_{FL} of 0.88% and 0.53% in the solid-state, respectively, compared to the ϕ_{FL} estimated in the solution-state in DIOX (16.20% for **PDI$_2$** and 3.77% for **PDI$_3$**). The lower ϕ_{FL} values of **PDI$_2$** and **PDI$_3$** in the solid-state indicate the presence of nonradiative decay channels involved in the excited-state dynamics of the PDI dimers in thin films.[16]

To obtain critical insights into the nonradiative decay pathways governing the excited-state dynamics of the PDI multichromophoric assemblies in the solid-state, we performed femtosecond transient absorption (fsTA) spectroscopic measurements of **PDI$_2$** and **PDI$_3$** in thin films in PMMA (Fig. 2). Upon photoexcitation at 480 nm with a 100 fs laser pulse, the fsTA spectra of **PDI$_2$** thin film depict negative ground-state bleach (GSB) and/or stimulated emission (SE) at ~540 to 610 nm and two distinct positive excited-state absorption (ESA) peaks centered at ~627 nm and ~707 nm (Fig. 2a). The observed twin ESA peaks at ~627 nm and ~707 nm correspond to the characteristic spectral signature of the perylenediimide radical cation ($PDI^{\bullet+}$) and radical anion ($PDI^{\bullet-}$), respectively.[12,13] The simultaneous occurrence of $PDI^{\bullet+}$ and $PDI^{\bullet-}$ transient features represent the CSS, confirming the SB-CS process in thin films of **PDI$_2$** in a nonpolar PMMA polymer matrix (ε = 2.80–3.20). At longer time delays of ~150 ps, the CSS state decays to a relaxed CSS state (**CSS$_{rel}$**) with non-negligible blue-shifted ESA features. Similar excited-state dynamics were observed for **PDI$_3$** thin film in PMMA upon photoexcitation at 480 nm. The fsTA spectra of **PDI$_3$** thin film depict GSB and/or SE at ~500 to 555 nm and ESA peaks at ~619 nm and ~698 nm (Fig. 2d). The two distinct ESA peaks characterize the unique spectral feature of $PDI^{\bullet+}$ and $PDI^{\bullet-}$, confirming SB-CS in thin films of **PDI$_3$** in PMMA.[12,13] The CSS state in **PDI$_3$** decays to a **CSS$_{rel}$** state with blue-shifted ESA peaks at higher time delays of ~150 ps.

Global analysis was applied to the fsTA data of **PDI$_2$** and **PDI$_3$** thin films to extract the evolution-associated spectra (EAS) and the corresponding population dynamics of the excited-states involved in the above-mentioned transformations. Representative kinetic traces at selected wavelengths, along with the globally fitted curves, are shown in Fig. S21a and b to illustrate the accuracy of the fit. The EAS and the relative population profile of **PDI$_2$** demonstrated two principal components (Fig. 2b and c). The first component (A) is assigned to the CSS state formed due to SB-CS. The CSS state undergoes rapid vibrational relaxation (τ_{VR} = 91.3 ps) to form the second principal component (B). The component (B) is assigned to a **CSS$_{rel}$** state, which decays to the ground-state *via* charge recombination (CR) with a time constant of τ_{CR} = 1.10 ns. Likewise, the EAS and the relative population profile of **PDI$_3$** exhibited two principal components (Fig. 2e and f). The first principal component (A) is attributed to the CSS state. The CSS state in **PDI$_3$** decays *via* vibrational relaxation (τ_{VR} = 100.5 ps) to form the **CSS$_{rel}$**. Further, the **CSS$_{rel}$** decays to the ground-state *via* CR within τ_{CR} = 1.07 ns. The immediate appearance of the CSS feature upon photoexcitation shows that ultrafast CS occurs for **PDI$_2$** and **PDI$_3$** in the solid-state within the ~110 fs instrument response.[12,13,15] Recently, we have reported SB-CS in monomeric solutions of **PDI$_2$** and **PDI$_3$** in a polar solvent like acetone.[16,17] The experimentally determined CS time constants in acetone were τ_{CS} = 6.3 ps and 3.7 ps for **PDI$_2$** and **PDI$_3$**, respectively. Notably, the SB-CS dynamics observed in the solid-state for both molecules in this work are approximately an order of magnitude faster than those measured in solution. This could be due to the angular molecular design of **PDI$_2$** and **PDI$_3$**, with core-twisted PDI units, which compels the molecules to arrange in a J-aggregate type solid-state packing, promoting the long-range quadrupolar effects[13,15,20] and short-range intermolecular π–π interactions[12,21,22] necessary for efficient charge separation in the solid-state. Additionally, to understand the matrix effects modulating the aggregation process, favouring ultrafast SB-CS in the solid-state, we probed the feasibility of SB-CS in **PDI$_2$** and **PDI$_3$** in another nonpolar (ε = 2.60) polymer matrix, polystyrene (PS). The deconvoluted fsTA spectra showed the population of a broad singlet excited-state with partial charge transfer character (Fig. S22).[13] The absence of the distinct ESA features of the CSS in the fsTA spectra confirmed

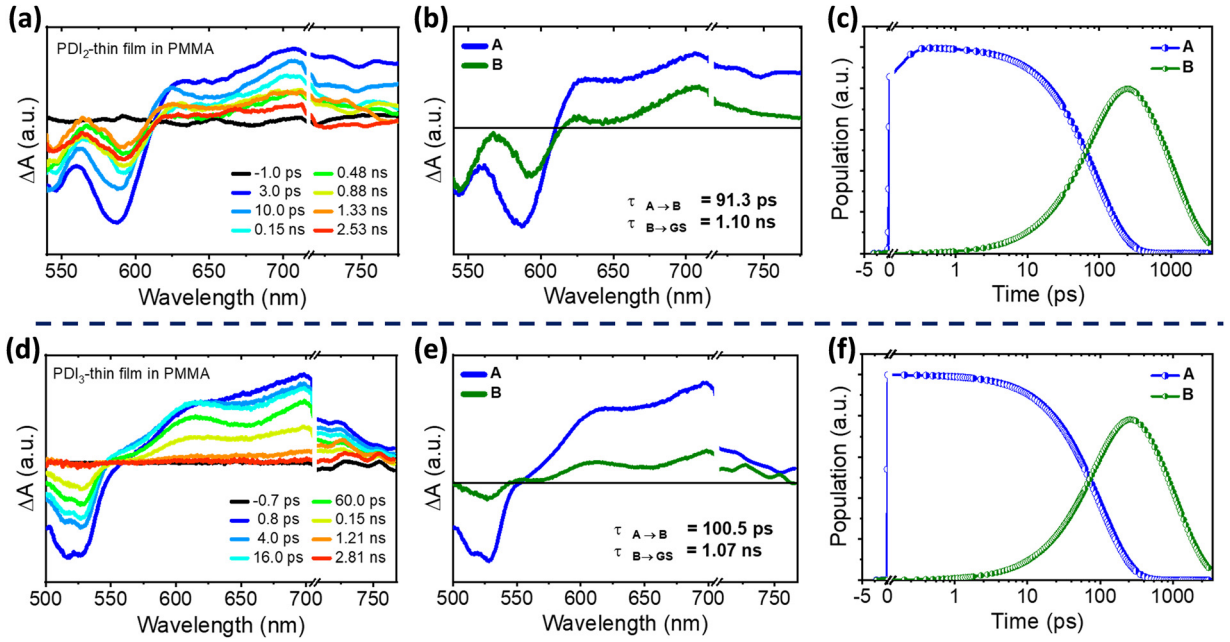

Fig. 2 fsTA spectra of (a) **PDI$_2$** and (d) **PDI$_3$** in thin films in PMMA showing the excited-state dynamics upon photoexcitation. EAS reconstructed from global analysis of the fsTA data of (b) **PDI$_2$** and (e) **PDI$_3$** with the A → B → GS kinetic model, where A is the CSS, B is the **CSS$_{rel}$**, and GS is the ground state (λ_{ex} = 480 nm). Relative population profile of the excited-states fitted using the above kinetic models in (c) **PDI$_2$** and (f) **PDI$_3$**.

the infeasibility of SB-CS in **PDI$_2$** and **PDI$_3$** thin films in PS (refer to SI for more details). The above result sheds light on the crucial role played by PMMA in providing an optimum dielectric environment and promoting favourable solid-state packing necessary for ultrafast SB-CS.

Further, we measured the fluorescence lifetimes of **PDI$_2$** and **PDI$_3$** thin films in PMMA (Fig. S23 and S24). The major fluorescence lifetime component in **PDI$_2$** ($\tau_{FL}^{PDI_2}$ = 2.63 ns (71%)) and **PDI$_3$** ($\tau_{FL}^{PDI_3}$ = 2.60 ns (73%)) is in reasonable agreement with the decay constants for the **CSS$_{rel}$** state in **PDI$_2$** and **PDI$_3$** obtained from the global analysis fits of the solid-state fsTA data in PMMA (refer to SI for more details).

To understand the arrangement and packing of the individual monomers in the aggregate structure contributing to the experimentally observed SB-CS dynamics, we optimized the **PDI$_2$** and **PDI$_3$** aggregate ground-state geometries using DFT at the B3LYP-D3/6-31G level of theory in Gaussian 16. The optimizations were carried out employing a dimer model in vacuum. The optimized structure of **PDI$_2$** aggregate exhibited a slip-stacked orientation between the monomers, where the two planar PDI fragments are forced to arrange in a head-to-tail fashion due to the ineffective stacking of the core-twisted PDI fragments (Fig. S25a). Comparably, the optimized structure of **PDI$_3$** aggregate showed a slip-stacked arrangement between the central PDI fragments (Fig. S25b). The interplanar distance between the slip-stacked PDI fragments was computed to be $d_{interplanar}$ = 3.30 Å and 3.66 Å in **PDI$_2$** and **PDI$_3$** aggregates, respectively (Fig. S25a and b).

To comprehend the role of intermolecular excitonic interactions intrinsic to the spatial chromophore arrangement and packing in the aggregate structure, we theoretically computed the long-range Coulombic coupling (J_{Coul}) and the short-range charge transfer-mediated coupling (J_{CT}) interactions in **PDI$_2$** and **PDI$_3$** aggregates (Table S1). The J_{Coul} interactions were computed for the singlet excited-state with highest oscillator strength (f) at the CAM-B3LYP-D3/DEF2-TZVP level of theory using excitation energy transfer (EET) method in Gaussian 16 (Fig. S26a, b and Table S2).[23,24] **PDI$_2$** and **PDI$_3$** exhibited comparable J_{Coul} values of −732.76 cm^{-1} and −710.30 cm^{-1}, respectively. The negative J_{Coul} values reinstate the J-type dipole–dipole excitonic interactions operative in the self-assembled aggregate structures of **PDI$_2$** and **PDI$_3$**.[19,25,26] In molecular aggregates, charge transfer (CT) plays a critical role in excitonic coupling and dictating the optical properties of the aggregates.[27,28] J_{CT} was calculated according to the equation S3 given in supporting information. **PDI$_2$** aggregate showed a significant J_{CT} of −85.22 cm^{-1}, whereas **PDI$_3$** aggregate exhibited weaker CT interactions, amounting to a J_{CT} of 37.92 cm^{-1}. The smaller $d_{interplanar}$ of 3.30 Å (Fig. S25a) and the effective HOMO-HOMO/LUMO-LUMO overlap (Fig. S27) between the J-type dimer stacks in **PDI$_2$** aggregate structure contribute to the theoretically observed higher strength of CT interactions. On the contrary, the larger $d_{interplanar}$ of 3.66 Å (Fig. S25b) and the poor HOMO–HOMO/LUMO–LUMO overlap (Fig. S28) between the J-type dimer stacks in **PDI$_3$** aggregate structure could be responsible for the lower strength of CT interactions.[19] According to equation S4, the total excitonic coupling (J_{Total}), was estimated to be −817.98 cm^{-1} and −672.38 cm^{-1} in **PDI$_2$** and **PDI$_3$** aggregates, respectively.

A plausible schematic Jablonski diagram summarizing the mechanism of the SB-CS dynamics in **PDI$_2$** and **PDI$_3$** upon photoexcitation is shown in Fig. 3. Compared to the S_1* state

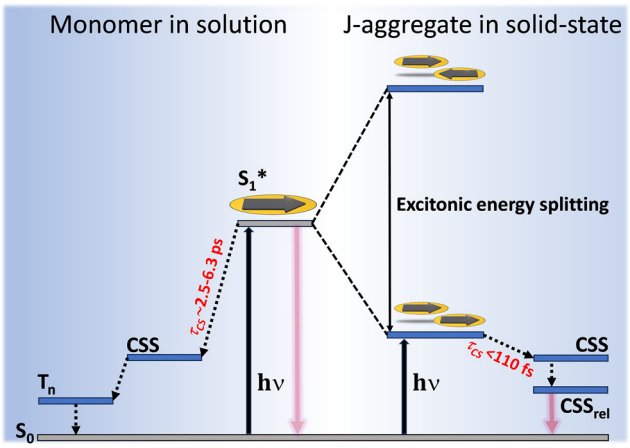

Fig. 3 Schematic energy profile diagram summarizing the excited-state dynamics of **PDI_2** and **PDI_3** in (left) solution as monomer and (right) thin films in PMMA; S_0 = ground-state, S_1* = singlet excited-state; CSS = charge separated state; **CSS_{rel}** = relaxed charge separated state; T_n = triplet excited-state. N. B.- The solution-state photophysics is adapted from the previously reported energy profile diagrams.[16,17]

energy in solution, **PDI_2** and **PDI_3** exhibit a J-type excitonic energy splitting upon aggregation in the solid-state. The initially populated excited-state shows an order of magnitude faster charge separation in the solid-state compared to solution, populating the CSS *via* SB-CS. In the solid-state, the CSS relaxes to a lower vibrational energy level (**CSS_{rel}**), which recombines radiatively to repopulate the ground-state, whereas in solution, triplet excited-states are populated.[16,17]

In summary, we have demonstrated ultrafast symmetry-breaking charge separation (SB-CS) in angularly oriented PDI multimers in the solid-state. A perylenediimide dimer (**PDI_2**) and a trimer (**PDI_3**) were prepared with systematic enhancement of core-twisted PDI fragments. Excitation and emission spectra of **PDI_2** and **PDI_3** thin films in a nonpolar polymethyl methacrylate (PMMA) polymer matrix exhibited broad red-shifted excitation and emission bands compared to the monomer photophysical properties in DIOX solvent. The red-shifted excitation spectra of **PDI_2** and **PDI_3** thin films relative to their monomeric counterparts in DIOX, suggest the emergence of J-type aggregates in the solid-state assemblies of these chromophores. Solid-state fsTA measurements of **PDI_2** and **PDI_3** in thin films in PMMA matrix exhibited ultrafast charge separation within the instrument response function (τ_{CS} <110 fs). The optimized dimer structures of the PDI aggregates corroborated the formation of J-type slip-stacked architectures. Theoretical calculations substantiated the role of through-space long-range intermolecular excitonic communication and short-range π–π interactions in the solid-state molecular packing driving the ultrafast charge separation process. Therefore, this investigation could be beneficial for designing SB-CS materials capable of solid-state charge separation for advanced optoelectronic devices.

M. H. acknowledges the Science and Engineering Research Board (CRG/2023/005859), Department of Science and Technology, Govt. of India, for financial support. We greatly acknowledge the support for high-performance computing time at the Padmanabha cluster, IISER TVM, India. A. M., A. T., and P. D. M. thank IISER TVM for the financial support. K. V. and A. R. acknowledge CSIR and UGC, respectively, for financial assistance.

Conflicts of interest

There are no conflicts to declare.

Data availability

All the experimental and theoretical data are provided in the supplementary information (SI). Supplementary information is available. See DOI: https://doi.org/10.1039/d5cc04382d.

References

1 E. Sebastian and M. Hariharan, *ACS Energy Lett.*, 2022, **7**, 696–711.
2 A. N. Bartynski, M. Gruber, S. Das, S. Rangan, S. Mollinger, C. Trinh, S. E. Bradforth, K. Vandewal, A. Salleo, R. A. Bartynski, W. Bruetting and M. E. Thompson, *J. Am. Chem. Soc.*, 2015, **137**, 5397–5405.
3 C. Lin, T. Kim, J. D. Schultz, R. M. Young and M. R. Wasielewski, *Nat. Chem.*, 2022, **14**, 786–793.
4 Y. Guo, Z. Ma, X. Niu, W. Zhang, M. Tao, Q. Guo, Z. Wang and A. Xia, *J. Am. Chem. Soc.*, 2019, **141**, 12789–12796.
5 E. Vauthey, *Chem. Phys. Chem.*, 2012, **13**, 2001–2011.
6 M. J. Álvaro-Martins, C. Billiaux, P. Godard, R. Oda, G. Raffy and D. M. Bassani, *Chem. Commun.*, 2023, **59**, 7963–7966.
7 A. I. Ivanov, *J. Photochem. Photobiol. C*, 2024, **58**, 100651.
8 F. C. Spano, *J. Phys. Chem. C*, 2024, **128**, 248–260.
9 R. M. Young and M. R. Wasielewski, *Acc. Chem. Res.*, 2020, **53**, 1957–1968.
10 A. Nowak-Król and F. Würthner, *Org. Chem. Front.*, 2019, **6**, 1272–1318.
11 J. Kong, W. Zhang, G. Li, D. Huo, Y. Guo, X. Niu, Y. Wan, B. Tang and A. Xia, *J. Phys. Chem. Lett.*, 2020, **11**, 10329–10339.
12 J. Mao, Q. Fan, Z. Yan, X. Chen, S. Zhao, Y. Lu, S. Li, W. Jiang, Z. Xu, Z. Wang and J. Wang, *J. Am. Chem. Soc.*, 2025, **147**, 12730–12739.
13 C. E. Ramirez, S. Chen, N. E. Powers-Riggs, I. Schlesinger, R. M. Young and M. R. Wasielewski, *J. Am. Chem. Soc.*, 2020, **142**, 18243–18250.
14 G. Ran, J. Zeb, Y. Song, P. A. Denis, U. Ghani and W. Zhang, *J. Phys. Chem. C*, 2022, **126**, 3872–3880.
15 A. Khan, N. A. Tcyrulnikov, R. Roy, R. M. Young, M. R. Wasielewski and A. L. Koner, *J. Phys. Chem. C*, 2024, **128**, 10474–10482.
16 A. Mazumder, K. Vinod, A. C. Thomas and M. Hariharan, *J. Phys. Chem. Lett.*, 2025, **16**, 4819–4827.
17 A. Mazumder, K. Vinod, P. D. Maret, P. P. Das and M. Hariharan, *J. Phys. Chem. Lett.*, 2024, **15**, 5896–5904.
18 M. Hecht and F. Würthner, *Acc. Chem. Res.*, 2021, **54**, 18.
19 N. J. Hestand and F. C. Spano, *Chem. Rev.*, 2018, **118**, 7069–7163.
20 S. Seetharaman, N. Zink-Lorre, D. Gutiérrez-Moreno, P. A. Karr, F. Fernández-Lázaro and F. D'Souza, *Chem. – Eur. J.*, 2022, **28**, e202104574.
21 P. J. Brown, M. L. Williams, S. B. Tyndall, Y. Qi, R. M. Young and M. R. Wasielewski, *J. Phys. Chem. C*, 2024, **128**, 14185–14194.
22 R. R. Kaswan, D. Molina, L. Ferrer-López, J. Ortiz, P. A. Karr, Á. Sastre-Santos and F. D'Souza, *Angew. Chem., Int. Ed.*, 2025, **64**, e202502516.
23 G. D. Scholes and K. P. Ghiggino, *J. Phys. Chem.*, 1994, **98**, 4580–4590.
24 Z. Q. You and C. P. Hsu, *Int. J. Quantum Chem.*, 2014, **114**, 102–115.
25 M. Kasha, H. R. Rawls and M. A. El-Bayoumi, *Pure Appl. Chem.*, 1965, **11**, 371–392.
26 A. S. Davydov, *Phys.-Usp.*, 1964, **7**, 145–178.
27 M. Mandal, S. Mardanya, A. Saha, M. Singh, S. Ghosh, T. Chatterjee, R. Patra, S. Bhunia, S. Mandal, S. Mukherjee, R. Debnath, C. M. Reddy, M. Das and P. K. Mandal, *Chem. Sci.*, 2025, **16**, 901–909.
28 X. Chang, M. Balooch Qarai and F. C. Spano, *J. Phys. Chem. C*, 2022, **126**, 18784–18795.

